Redox dynamics of subduction revealed by arsenic in serpentinite

G.S. Pokrovski, C. Sanchez-Valle, S. Guillot, A.Y. Borisova, M. Muñoz, A.-L. Auzende, O. Proux, J. Roux, J.-L. Hazemann, D. Testemale, Y.V. Shvarov

Supplementary Information

The Supplementary Information includes:

- Materials and Methods
- Tables S-1 to S-6
- Figures S-1 to S-5
- Supplementary Information References

Materials and Methods

Serpentinite samples and geodynamic setting

The geodynamic setting, *T-P*-time evolution, and geochemical and petrological features of the Tso Morari serpentinites have thoroughly been described elsewhere (Guillot *et al*., 2000, 2001, 2008; Hattori and Guillot, 2003, 2007; Deschamps *et al*., 2010 and references therein). Briefly, these rocks originate from the forearc mantle overlying the northward subducting Neo-Tethys lithosphere and the margin of the Indian continent. They are associated with the eclogites of the Tso-Morari ultra high-pressure metamorphic unit that was once a shallow-water sedimentary sequence prior to being subducted beneath Eurasia at ~55 Ma. The unit reached ~100 km depth and ~650 °C before being exhumed together with serpentinites at ~50 Ma. The *T-P*-time trajectory of the rocks has been thoroughly reconstructed using a range of petrological, geochronological and thermobarometric indicators (*e.g.*, Guillot *et al*., 2008; Soret *et al*., 2021 and references therein). They suggest rapid cooling and fast exhumation after the peak metamorphism. The serpentinite rocks are dominated by antigorite with subordinate magnetite, secondary olivine, occasional chromite, and minor later chrysotile, lizardite, calcite, and talc. The distinguishing feature of these serpentinites is their strong enrichment in As, Sb, B, Li, Pb, and U compared to mantle peridotites; this enrichment was likely due to sediment-derived aqueous fluids and/or seawater at early stages of subduction (see Deschamps *et al*., 2010 for detailed petrological and geochemical description). Another key feature of these rocks is their pristine deep imprint and the absence of any indication of (near)surface oxidation (*e.g.*, complete absence of hematite, goethite, or clay minerals). The major chemical and mineralogical characteristics of the investigated samples, relevant to the present study, are summarised in Table S-1.

Samples of the CH series are from Deschamps *et al.* (2010). Samples of the TSL series were collected in a later campaign from the same locality, and selectively characterised in the present work using a range of laboratory techniques such as optical microscopy (OM), powder X-ray diffraction (XRD), scanning electron microscopy (SEM), bulk-rock chemical analyses (BR), electron probe micro analyser (EPMA), and laser ablation inductively coupled plasma mass spectrometry (LA-ICPMS), following established protocols (*e.g.*, Borisova *et al*., 2021; Pokrovski *et al*., 2021). Antigorite mineral fractions of samples TSL16 and TSL19 with strongly contrasting As redox state (Tables S-1, S-2) were additionally examined by transmission electron microscopy (TEM) following conventional methods described in Auzende *et al*. (2006).

X-ray absorption spectroscopy data collection

X-ray absorption spectroscopy (XAS) measurements at the Fe (7112 eV) and As (11867 eV) K-edges (including the X-ray absorption near-edge structure region - XANES, and the extended X-ray absorption fine structure region - EXAFS) were performed both on bulk serpentinite rocks and their antigorite-enriched and magnetite-enriched mineral fractions at BM30-FAME beamline at the European Synchrotron Radiation Facility, ESRF, Grenoble, France (Proux *et al*., 2005). Energy was selected using a liquid-nitrogen cooled Si(220) double-crystal monochromator with dynamic sagittal focusing. Unwanted high-energy photons (harmonics) were removed using two Rh-covered mirrors surrounding the monochromator; mirrors being also used to collimate the beam in the vertical direction (1st mirror) and to focus the beam in the same direction (2nd mirror). These optical elements yield a beam spot on the sample of 300 µm horizontal × 200 µm vertical (full width half maximum), an X-ray flux of 5 × 10^{11} (Fe K-edge) and 10^{12} (As K-edge) photons/s and an energy resolution close to the intrinsic resolution of the monochromator crystals (i.e. ~0.4 eV at Fe K-edge, ~0.6 eV at As K-edge). This setup allows acquisition of very good quality XANES and EXAFS spectra at concentrations as low as a few 10s of ppm As. Fluorescence spectra were collected in the right-angle geometry using a 30-element solid-state germanium detector (Canberra). Energy calibration of each scan was checked using the As_2O_3 (cubic, arsenolite)

and Fe metal references whose K-edge energies were set, respectively, to 11871.5 and 7112.0 eV as the maximum of the spectrum first derivative. The uncertainty of the energy position is <0.3 eV.

To prepare mineral-enriched fractions, antigorite crystals were hand-picked under a stereo microscope from mildly ground fresh pieces of serpentinite rocks, whereas magnetite grains were separated using a magnet. The magnetite-enriched fraction, however, inevitably contained some part of the antigorite matrix (up to ~10%) in which the magnetite grains were solidly embedded. Arsenic associated with magnetite-enriched fractions makes, however, a rather small contribution to total arsenic inventory in serpentinite (<5 % As_{tot}), both because of the low abundance of magnetite itself (average content in our samples is 1.8 ± 1.0 mol. %, 1 s.d. error) and associated relatively small As concentrations as determined by LA-ICPMS (Table S-1) and from X-ray fluorescence amplitude (Table S-2). These data show that magnetite would account for only ~0.02 (CH98B) to <10 % (TSL19) of total arsenic in our samples. To ensure homogeneity necessary for good quality spectra, fresh pieces of bulk rock and its mineral fractions were thoroughly ground under ethanol thereby avoiding any potential oxidation. The powders were dried under an N_2-atmosphere and pressed into 5-mm diameter pellets, which were placed in a liquid He cryostat (~10–15 K). The low temperature and inert atmosphere of the spectra acquisition setup were essential both to avoid potential X-ray beam-induced damage to redox-sensitive elements like As and Fe (Testemale *et al*., 2009, 2011; Borisova *et al*., 2010), and to significantly increase the signal-to-noise ratio of the EXAFS spectra by dampening thermal disorder. In addition, the beam position at the sample was slightly changed at each following scan to further reduce potential beam-redox artefacts. Before summing up, multiple scans were carefully examined and were found to be identical independently of beam-exposure time, thereby demonstrating that beam-induced changes were insignificant.

A large number of As reference compounds (Table S-2) was recorded, using the same protocol at liquid He temperature, to enable accurate and straightforward determination of As redox state using linear combination fit (LCF) analyses of As K-edge XANES spectra. Reference As aqueous solutions were also measured in cryostat in a frozen state with addition of small amounts of glycerine to avoid formation of ice crystals that may generate diffraction peaks in the EXAFS spectra. The iron redox ratio Fe^{III}/Fe^{II} (±0.05, 1 s.d. error) and Fe coordination in antigorite fractions were determined from the Fe K pre-edge and main-edge XANES features, using calibrations and numerical algorithms developed in Muñoz *et al*. (2013). Arsenic K-edge EXAFS spectra were analysed using the Horae software (Ravel and Newville, 2005) and following established protocols (Kelly *et al*., 2008; Borisova *et al*., 2010).

Our approach, combining macro-XAS measurements with micro-analytical laboratory techniques, is believed to be well-suited for the samples context of this study. The use of macroscopic mineral fractions and homogenised samples for XAS both allows the best representability of measurements at the rock-sample scale and enables the best quality XANES, and in particular, EXAFS spectra that are very sensitive to sample inhomogeneity. Note that these two critical aspects could not have been fulfilled using the X-ray micro-beam approach. It can be seen in Fig. 1 that our mineral grains are big enough (100–1000 µm in size) both to allow us to use physical mineral separation procedures and to enable *in situ* microanalytical elemental analyses (SEM, EPMA, LA-ICPMS) to ensure the grain homogeneity and representativeness across the given sample scale, and provide the necessary analytical sensitivity (*e.g.*, detection limits of <0.1 ppm for As by LA-ICPMS), unachievable at present using micro-beam XRF/XAS. Combined with other whole-rock and mineralogical analyses (Table S-1), our approach therefore allows us to place robust constraints on As and Fe mass and redox balance across the whole sample scale.

X-ray absorption spectroscopy results

The obtained structural data are reported in Tables S-2, S-3 and S-4, and representative XANES and EXAFS spectra of samples and reference compounds are shown in Figures 2 and S-1, respectively. As K-edge XANES LCF fits were performed using different structural and redox reference compounds listed in Table S-2. Best fits of the whole set

of samples were achieved using a combination of arsenide, nominally As^{-III} (NiAs, nickeline), arsenite, As^{III} (aqueous arsenious acid solutions), and arsenate, As^{V} (aqueous arsenic acid solutions or arsenate adsorbed on ferrihydrite or gibbsite, which exhibit very similar XANES spectra, but see below for EXAFS). Neither native arsenic nor arsenic sulfides (As_2S_3, FeAsS) were detected (detection limit <3 at. % As). Similarly, fits using As^{III} and As^{V} references compounds, in which the As absorber has closely spaced second-shell heavy atoms such as As or Fe (*e.g.*, arsenolite, As_2O_3, Testemale *et al.*, 2004; As^{V} partially incorporated into magnetite structure, van Genuchten *et al.*, 2019, 2020), could not match the post white-line XANES spectral part of our antigorite and magnetite samples (see also Fig. 2, main text). This result suggests that oxidised As is unlikely to be hosted in the structural sites of both minerals, nor does forms arsenic own oxide or metal arsenate phases.

Analyses of EXAFS spectra show that in arsenide-free antigorite (ant) and magnetite-enriched (mt) samples (*e.g.*, CH98A, TSL16), the EXAFS signal is largely dominated by the first atomic shell of oxygen atoms corresponding to [AsO_3] and [AsO_4] moieties. Quantitative EXAFS analysis for As^{III}/As^{V}-dominated samples yields 3 to 4 oxygen atoms at mean As-O distances between 1.69 and 1.75 Å (±0.02 Å), demonstrating a mixture of $As^{III}O_3$ and $As^{V}O_4$ types of species. In arsenide-bearing samples, part of As is directly bound to Ni (*e.g.*, sample TSL19, As-Ni distance = 2.45 ± 0.02 Å, As-Ni coordination number = 3 ± 0.5; Table S-3), indicating the presence of nickel arsenide phases (NiAs-like). The remaining As atoms are bound to O (or OH groups, H atoms being too light to be detected by XAS) as arsenate ($As^{V}O_4$), in quantitative agreement with the XANES results (see Fig. 1). The very weak (if any) EXAFS signal arising from outer-shell atomic neighbours in As^{III}/As^{V}-bearing antigorite (and magnetite, see below) fractions indicates disordered second shell coordination environments, likely composed of relatively light cations (Al, Mg, $R_{As\text{-}Mg} \approx 2.7$–2.9 Å) and weak multiple scattering contributions within the AsO_4 tetrahedron (MS), similar to those from As surface-sorbed complexes on gibbsite (Fig. S-1). Neither 2nd shell Fe (or another heavy metal, *e.g.*, Ni, Cr, As), nor Si or Mg contributions from adjacent structural Si or Mg atoms ($R_{As\text{-}Si} \approx 3.2$–3.3 Å; $R_{As\text{-}Mg} \approx 3.4$–3.5 Å), which would arise in case of As entering the anionic (Si,As)O_4 structural sites, could be detected. This result suggests that As is unlikely to substitute for Si in antigorite. Furthermore, a lack of correlation of different As redox fractions or total As contents with the Fe^{III} fraction or Al^{III} content in antigorite (Figs. S-3 and S-4), along with the absence of As-O-As bond contributions in the EXAFS spectra, does not support charge-compensated substitution mechanisms such as $As^{V} + As^{III} = 2Si^{IV}$ or $As^{V} + Fe^{III}/Al^{III} = 2Si^{IV}$. In addition, the absence of correlations of total As contents with those of other trace/minor elements of comparable concentrations (*e.g.*, Al, V, Ni, Na, B; *e.g.*, Fig. S-3) that commonly enter the antigorite structural sites further points to a different, likely site-unspecific, As^{III} and As^{V} position in the mineral. Our XANES and EXAFS analysis is thus more consistent with both [$As^{V}O_4H_n^{n-3}$] and [$As^{III}O_3H_n^{n-3}$] oxyanions being incorporated in-between antigorite structural layers or in structural defects and imperfections and loosely bound to [MgO_6] cationic sheets, rather than with direct isomorphic substitution of As for Si in SiO_4 tetrahedrons or for Mg in MgO_6 octahedra.

Like for antigorite, our EXAFS data clearly rule out incorporation of As^{III} and As^{V} into the magnetite structural sites or adsorption as stable inner-sphere complexes on the mineral surface. It can be seen in Figure S-1 that the As K-edge EXAFS spectra of magnetite-enriched fractions are completely devoid of the pronounced second-shell signals typical of arsenate absorbed onto Fe^{III} oxyhydroxide minerals (strong As-O-Fe bonds, *e.g.*, Cancès *et al.*, 2005) and of arsenate incorporated into tetrahedral (Fe,As)O_4 structural sites of low-temperature magnetite in which the AsO_4 tetrahedron was shown to be surrounded by 6 to 12 second-shell Fe atoms at 3.4–3.6 Å, giving rise to an intense 2nd-shell contribution in the EXAFS spectrum (*e.g.*, van Genuchten *et al.*, 2019, 2020); see the "TSL16 mt" sample compared to the "As^{V} on ferrihydrite" and "As^{V} in magnetite" standards in Figure S-1.

Notes on the available data on arsenic incorporation in serpentine-like minerals and magnetite

Our findings of non-specific incorporation of oxidised arsenic in antigorite and magnetite allow us to explore the concept that the As^{III}/As^{V} ratio in the mineral may directly reflect that in the coexisting aqueous fluid. The few direct available data of arsenic incorporation into silicate minerals seem to support this concept as discussed below.

Our structural data are in agreement with direct laboratory experiments of olivine serpentinisation in aqueous alkaline solutions at 200 °C suggesting As^{V} sorption on the formed serpentinite, rather than its incorporation into SiO_4 structural sites (Lafay *et al*., 2016). However, another experimental study by Ryan *et al*. (2019), devoted to the synthesis of serpentinite from alkaline Mg-, Si-, Al- and As-bearing aqueous solutions at 200 °C, reported formation of As^{III}- and As^{V}-bearing serpentinites with up to 1 wt. % As. These authors postulated that both As^{III} and As^{V} substitute for SiO_4 in the tetrahedral sheets of the mineral, but direct evidence for such a mechanism remained elusive. The lack of stoichiometric (*i.e*. the presence of talc interlayers) and charge balance in the synthesised As-substituted serpentinite compositions, the absence of correlation with Al content, and the very weak 2nd shell signal in their reported single EXAFS spectrum, which is similar to our spectra (Fig. S-1), all these features do not support As substitution in Si structural sites. In addition, based on general isomorphic substitution rules, the tetrahedral $As^{V}O_4$ moiety should have a much greater ability than its trigonal pyramidal $As^{III}O_3$ counterpart to substitute for tetrahedral SiO_4. Therefore, it should normally be expected that As^{V} would strongly enrich the synthetic serpentines compared to As^{III}, if arsenic were to substitute for Si. This was not, however, observed in Ryan *et al.*'s (2019) study, with equally significant fractions of As^{III} present in the synthetic products. The largest As^{V}/As^{III} ratio was 4:1, as reported in a single sample investigated using XAS in their study, which was synthesised from a solution containing equal amounts of As^{V} and As^{III}. Such fractionation seems to be too weak to support an isomorphic substitution mechanism for As^{V}. More likely, such modest fractionations would be due to sorption processes, with slightly preferential sorption on the mineral surface of the stronger charged arsenate ion ($As^{V}O_4^{3-}$) *vs*. the arsenite ion ($As^{III}O(OH)_2^{-}$) that are expected to be the dominant As^{V} and As^{III} species, respectively, in the highly alkaline solution used in Ryan *et al.*'s (2019) synthesis. In contrast to their study, the predominance of uncharged or weakly charged As^{III} and As^{V} oxyhydroxide complexes, as shown by fluid speciation calculations at the serpentinisation conditions of our study (see below and Fig. S-5), would further hamper both arsenite and arsenate substitution for SiO_4^{4-} tetrahedrons in the antigorite structure. Other literature data on As intake by aluminosilicate minerals, such as kaolinite, montmorillonite and micas at near-ambient conditions obtained by XAS (Foster and Kim, 2014 and references therein), collectively point to rather minor differences in As^{III} *vs*. As^{V} affinities for their sorption on the mineral surfaces, with dominant formation of outer-sphere arsenate and arsenite complexes.

Although no direct experimental data are available, to the best of our knowledge, on As incorporation into magnetite at hydrothermal conditions, our XAS analysis above clearly rules out As^{V} preferential incorporation in magnetite. This finding apparently contrasts to available reports on partial As^{V} incorporation into the $Fe^{III}O_4$ tetrahedral sites of nano-crystalline magnetite synthesised at ambient laboratory conditions by bacteria-mediated or chemical reduction of Fe^{III} oxyhydroxides, As^{V}-Fe^{III} co-precipitation or electrochemical Fe^{0} oxidation (*e.g.*, Coker *et al*., 2006; Huhmann *et al*., 2017; van Genuchten *et al*., 2019, 2020). However, the conditions of those low-temperature experiments are very different from those of subduction-zone contexts. Multiple instances of direct and complementary evidence provided in this study rule out a significant role of magnetite as the As^{V} host both in the context of our study and, more generally, for hydrothermal-metamorphic environments. This evidence includes *i)* the lack of 2nd shell Fe contribution in our As EXAFS spectra of magnetite-enriched fractions and their great spectral similarity with antigorite (Fig. S-1); *ii*) the absence of any specific correlations of As concentrations with those of elements entering the magnetite structure (*e.g*., Al, V, Co; Fig. S-4); *iii*) the absence of any significant relationship between the As^{V} fraction and magnetite abundance in the serpentinite rock or Fe^{III} fraction in serpentinite (Fig. S-4); *iv*) mass balance estimations showing the major part of As^{III} and As^{V} to be hosted by antigorite, and *v)* the extensive data sets from a variety of high-temperature

hydrothermal and metamorphic environments showing that magnetite is a poor host of arsenic, often displaying concentrations below typical detection limits of few ppm As for LA-ICPMS (*e.g.*, Nadoll *et al.*, 2014), despite the ubiquity of As in hydrothermal fluids (up to 100–1000 ppm As, *e.g.*, Kouzmanov and Pokrovski, 2012).

Thus, our spectroscopic and analytical data, coupled with a critical analysis of literature data, collectively suggest that both As^{III} and As^{V}, as oxyhydroxide anions of arsenious and arsenic acids in aqueous solution (*e.g.*, Perfetti *et al.*, 2008; Testemale *et al.*, 2011), are likely to be adsorbed from the aqueous fluid and incorporated with minimal fractionation into antigorite (and magnetite), *e.g.*, in structural defects and vacancies or in-between Mg-Si cation-anion layers, during the mineral (re)growth, (re)crystallisation or partial (re)dissolution during subduction. In light of these results, pointing to fairly comparable incorporation degrees of As^{III} and As^{V} in serpentinite from aqueous fluid, it would be plausible to assume that the As^{V}/As^{III} ratio in the fluid should reflect that in serpentinite. Therefore, this ratio in both minerals may be used as an indicator of redox conditions in the fluid. This concept is placed in a more quantitative physical-chemical framework in the following sections.

Thermodynamic modelling

Thermodynamic simulations of arsenic solubility and speciation in serpentinisation processes, along the subduction *T-P* path in the geodynamic and geochemical context of the Tso Morari rocks (Guillot *et al.*, 2008 and references therein), were performed in a model harzburgite-sediment-fluid system in a wide range of initial rock/fluid ratios (Table S-6). Calculations were carried out using the HCh package (Shvarov, 2008) enabling extension of the HKF model of aqueous species to the high pressures of the subduction context (up to ~60 kbar; Sverjensky *et al.*, 2014), and employing up-to-date revised thermodynamic datasets for arsenic- and nickel-bearing species and solid phases, major fluid components, rock-forming minerals and their solid solutions, and well-established activity coefficient models (Table S-5).

In particular, we included a variety of As/Ni-bearing minerals with robust thermodynamic data (Gamsjäger et *al.*, 2005) and a complete set of aqueous As^{III} and As^{V} oxyhydroxide species with well-constrained thermodynamic properties, which have been omitted in previous thermodynamic modelling studies of serpentinisation processes. Figure S-5 shows the distribution of these species in the fluid from the simulation exemplified in Fig. 3 in the main text. Note that robust HKF-model parameters for the $As(OH)_3^0$ and $AsO(OH)_3^0$ species, which are needed for reliable extrapolations to the *T-P* conditions of the present study, were derived from direct colorimetric and densimetric measurements of the partial heat capacity and volume of arsenious and arsenic acid solutions to 350 °C and 300 bar (Perfetti *et al.*, 2008). Likewise, the HKF-model parameters of arsenate and arsenite anions were derived from the measurements of $As(OH)_3^0$ and $AsO(OH)_3^0$ dissociation constants available to at least 100–200 °C and extrapolated to high *T-P* conditions using the well-constrained correlations of the HKF coefficients for anionic species (Shock *et al.*, 1997; Perfetti *et al.*, 2008). Arsenate and arsenite ion pairs with mono- and divalent alkali and alkali-earth cations (Na, K, Ca, Mg, and Fe) with recently published HKF-parameter estimations (Marini and Accornero, 2010) were also tested. Note that these estimations are exclusively based on rare ambient *T-P* data and/or inter-species correlations. These ion pairs were found to be negligible compared to the oxyhydroxide species in our low-salinity solutions. The single exception was the $KAsO_4^{2-}$ ion pair whose predicted association constants were more than 4 log units higher at $T > 400$ °C than that for analogous, and far better constrained, $NaAsO_4^{2-}$. In light of such inconsistencies and the lack of direct experimental data on the $KAsO_4^{2-}$ species, its available HKF thermodynamic parameters are likely unreliable and thus were ignored in the present modelling. Arsenic sulfide complexes, known in low-temperature geothermal springs and anoxic H_2S-rich (near)surface waters (*e.g.*, Keller *et al.*, 2014 and references therein), were not included in the modelling because there are currently no thermodynamic data allowing quantitative calculations of their abundances above ~150 °C. Tentative extrapolations of these data to moderate-temperature fluids (~300 °C), along with rare direct experiments

(*e.g.*, Pokrovski *et al.*, 1996, 2002 and references therein), indicate that such complexes would be negligible under most hydrothermal conditions above 200–300 °C. These data are also in line with the fundamental tendency of weakening covalent metal-sulfur bonds (As-S) while strengthening more ionic As-O bonds with increasing temperature (*e.g.*, Crerar *et al.*, 1985), thereby making As-O oxy-hydroxide complexes far more stable in aqueous solution at elevated temperatures of our subduction zone contexts. Our modelling predicts that nickel arsenides, orcelite (Ni_5As_2) and maucherite (Ni_8As_{11}), are the only As-bearing phases to form in our subduction context. No As-bearing pyrite, arsenopyrite or other arsenic sulfide phases (*e.g.*, AsS, As_2S_3) were predicted to precipitate. These predictions are in agreement with the absence of such phases in the serpentinite samples of this study and the very low total sulfur concentrations (<0.01 wt. %) in the bulk rock (Table S-1).

Aqueous Fe species for which reliable high *T-P* thermodynamic data are available (Table S-5) were also included in the modelling. Among them, the dominant Fe species were predicted to be Fe^{II} chlorides and hydroxides ($FeCl_2$ and $HFeO_2^-$) and Fe^{III} hydroxides ($Fe(OH)_4^-$). Ferrous sulfate and carbonate complexes were hypothesised in subduction zone fluids to explain Fe isotope ratios (*e.g.*, Debret *et al.*, 2016, 2020). However, there are no thermodynamic data for aqueous Fe^{II} and Fe^{III} carbonate and sulfate complexes that may actually allow their abundance to be predicted at the subduction zone conditions of the present study. Considering the relative stabilities of Cl-CO_3-SO_4 complexes known at near-ambient conditions, combined with generally lower abundances of sulfate and carbonate ligands than chlorides in hydrothermal-metamorphic fluids, it is expected that the abundances of Fe sulfate and carbonate complexes may be comparable with those of chlorides and hydroxides. However, the amount of total dissolved Fe in the fluid would always be largely inferior to that of Fe in the rock (*e.g.*, Fig. S-5).

Magnesium antigorite endmember was found to be the thermodynamically stable polymorph amongst the other Mg-serpentine polymorphs such as chrysotile and lizardite that are more common in lower *T-P* serpentinisation settings. Although the transformation of those phases to antigorite upon subduction may release small amounts of water, silica and some trace elements, and slightly modify the Fe^{II}/Fe^{III} ratio in the mineral and proportions of accompanying minerals such as magnetite (*e.g.*, Kodolányi and Pettke, 2011; Vils *et al.*, 2011; Evans *et al.*, 2012; Schwartz *et al.*, 2013), this transition has a minor effect on the redox state of the bulk system considered in this study. We also included estimations of the properties of Fe^{III}-bearing antigorite and chrysotile, based on mineral exchange reactions and polyhedral contribution approaches (see Table S-5 for details and references). Our data are in agreement with the rare early estimations (*e.g.*, Klein *et al.*, 2009). Even though such estimations are subjected to potentially large uncertainties, the inclusion in the model of Fe^{III}, which represents the dominant Fe fraction in the studied natural serpentinites, enables far better constraints on Fe^{III} mass balance of the system dominated by antigorite. Our thermodynamic predictions (Fe^{III} = 20–80 % of total Fe in antigorite at T > 550 °C) account well for the directly measured Fe^{III} fractions in antigorite from Fe K-edge XANES spectra (Fe^{III} = 40–70 %, Table S-4). Furthermore, the calculated antigorite Fe^{III} contents display similar temperature trends as those known in natural serpentinites from different subduction environments (Debret *et al.*, 2014), thereby independently confirming the temperature range of our serpentinite samples (~550–650 °C). Moreover, the thermodynamically predicted Mg# number of olivine formed by breakdown of serpentine above 600 °C (Mg# = 92–96) is in excellent agreement with the analysed values for secondary (*i.e.* metamorphic) olivine from Tso-Morari serpentinite rocks and other localities (Mg# = 92–98; *e.g.*, Hattori and Guillot, 2007; Deschamps *et al.*, 2010) while being distinctly different from that of mantle olivine (Mg# = 90, Table S-6). This result further supports the plausibleness of our thermodynamic model, and provides independent confirmation to the process of partial deserpentinisation evidenced by published geochemical and geodynamic data.

Assessment of oxygen fugacity in the fluid using arsenic redox state

Our calculations are in general agreement with previous experimental and thermodynamic modelling studies focused on major elements (*e.g.*, McCollom and Bach, 2009; Merkulova *et al*., 2016, 2017; Piccoli *et al*., 2019; Maurice *et al*., 2020; Evans and Frost, 2021 and references therein), predicting similar equilibrium mineral phases and compositions, and oxygen fugacity evolving roughly from FMQ–10 to FMQ–5 at relatively low-temperature serpentinisation step (<300 °C) to FMQ±2 at higher temperatures closer to the onset of serpentinite breakdown, depending on the harzburgite/pelite/fluid ratios and open (*i.e.* partial fluid escape) *vs.* closed system behaviour. However, equilibrium arsenic redox state and exact speciation were found to be very little dependent on the given scenario, with Ni(Fe) arsenide phases being systematically stable and weakly soluble below ~500 °C, and progressively dissolving with further temperature increase by releasing dominantly As^{III} oxyhydroxide species ($As(OH)_3$ and $AsO(OH)_2^-$) in the fluid phase (Fig. S-5a), with very little As^V corresponding to an equilibrium As^V/As^{III} ratio of 10^{-6} to 10^{-3} at *T-P* peak metamorphism of 600–700 °C and ~30 kbar (Fig. 3). These equilibrium thermodynamics predictions in the bulk system strongly differ from the XAS-measured As^V/As^{III} ratios in serpentinites (~0.4 to ~11, Tables S-1, S-2).

Assuming that the As^V/As^{III} ratio in serpentinite records that of the aqueous fluid, such differences between predictions and analyses are well beyond the potential uncertainties related to the thermodynamic properties of arsenic aqueous species. Their extrapolations to the investigated *T-P* conditions of the serpentinite peak metamorphism (~650 °C) would yield a plausible error of less than ±1 log unit for the As^V/As^{III} ratio. Additional uncertainties may arise from the relatively small differences in As^V *vs*. As^{III} fluid/mineral partition coefficients based on rare available experiments (*e.g.*, Ryan *et al.*, 2019; see discussion above), which are unlikely to exceed ±0.5 $\log(As^V/As^{III})$. These combined errors, which would plausibly amount ±2 $\log f_{O_2}$ units, cannot account for the high As^V/As^{III} ratios analysed in the mineral. We therefore suggest that these ratios rather record strongly oxidising conditions in the fluid phase, out of equilibrium with the dominant serpentinite rock. Such a fluid was temporarily created via focused release due to antigorite and magnetite partial breakdown occurred close to the peak metamorphism.

Given that redox equilibria between As aqueous species in the fluid phase are rapidly attained, oxygen fugacity values in the fluid in the 550–700 °C range may be estimated from redox reactions between the dominant aqueous As species (Fig. S-5) to match the measured As^{III}/As^V ratios preserved in serpentinite:

$$As^{III}O(OH)_2^- + ½\ O_2 = As^VO_2(OH)_2^- \quad \text{(Eq. S-1)}$$

$$As^{III}\ (OH)_3^0 + ½\ O_2 = As^VO_3(OH)^{2-} + 2\ H^+ \quad \text{(Eq. S-2)}$$

At constant fluid pH, which is buffered by fast reactions of proton exchange between the fluid and the Mg-Si minerals and therefore is not affected by local O_2 changes, these reactions may be collectively expressed in a general form such as

$$As^{III}(aq) + ½\ O_2 \rightarrow As^V(aq) \quad \text{(Eq. S-3)},$$

and thus

$$\log(f_{O_2})_{local} = 2\times[\log(As^V/As^{III})_{measured} - \log(As^V/As^{III})_{bulk\ equil}] + \log(f_{O_2})_{bulk\ equil} \quad \text{(Eq. S-4)},$$

where 'bulk equil' stands for equilibrium values calculated in the fluid assuming thermodynamic equilibrium within the bulk system. The derived local f_{O_2} values in the fluid range from FMQ+8 to FMQ+12, depending on the exact scenario of subduction and fluid/rock ratio.

Supplementary Tables

Table S-1 Key characteristics of serpentinite samples from the Tso-Morari massif investigated in this study.

Sample number[a]	Method	CH98A	CH98B	CH146	TSL16	TSL18	TSL19	TSL20
Coordinates		78.22E, 33.13N	78.22E, 33.13N	78.25E, 33.10N	78.25E, 33.10N	78.25E, 33.10N	78.25E, 33.10N	78.25E, 33.10N
Major minerals	OM, SEM	antigorite						
Subordinate minerals	OM, SEM	magnetite						
Occasional minerals (if any)	OM, SEM	metamorphic olivine, later chrysotile, chromite, calcite, talc						
SiO_2, wt. %	BR	35.1	40.2	40.6	39.8	–	40.7	–
MgO, wt. %	BR	40.0	41.8	36.7	37.6	–	38.2	–
Al_2O_3, wt. %	BR	0.54	0.37	0.77	1.39	–	0.88	–
Fe_2O_3 (total), wt. %	BR	6.83	7.54	7.59	8.31	–	7.53	–
Mt in bulk rock, mol. %	XRD	1.0	0.5	<0.3	2.2	2.4	1.4	3.7
Fe^{III} in antigorite, at. %	XANES	66	61	70	59	72	38	61
Ni in antigorite, ppm	EPMA	2255	2825	2260	2050	–	1820	–
Ni in mt embedded in ant, ppm	LA-ICPMS	–	60–260	–	–	–	5834	–
Si in mt embedded in ant, wt. %	LA-ICPMS	–	–	–	–	–	0.22–0.81	–
Mg in mt embedded in ant, wt. %	LA-ICPMS	–	–	–	–	–	0.25–1.5	–
As in serpentinite rock, ppm, mean	BR	80 [b]	65	6.7	28	–	127	–
As in antigorite, ppm, mean (range)	LA-ICPMS	25 (18–33)	34 (4–76)	7.5 (4–12)	–	–	15 (4–56)	–
As in mt embedded in ant, ppm (range)	LA-ICPMS	–	0.3-0.6	–	–	–	129 (2–470)	–
Ant in mt-rich fraction, wt. %	OM, SEM	<10	<10	<10	<10	<10	<10	<10
As^V relative to total As in serp, %	XANES	60	60	23	72	75	54	45
As^V/As^{III} in serp	XANES	1.6	1.5	0.4	2.6	3.0	>11	0.8
As^{-III} relative to total As in serp, %	XANES	<5	<3	22	<3	<3	43	<3

[a] Elemental composition for the CH series is adopted from Hattori and Guillot (2007) and Deschamps *et al*. (2010), and for the TLS-series from this study. [b] A value of 275 ppm As was reported for bulk-rock by Hattori *et al*. (2005) obtained by As extraction followed by atomic absorption spectroscopy. This value might be overestimated due to intrinsic limitations of the AAS analysis; alternatively, their sample might have contained traces of nickeline/pentlandite, (Fe,Ni)(S,As), with high As tenors (*cf*. Table 2 in Hattori *et al*., 2005). Total sulfur content in bulk-rock samples is <0.01 wt. %. Mineral abbreviations: serp = serpentinite rock, mt = magnetite, ant = antigorite. Method abbreviations: OM = optical microscopy; BR = bulk-rock chemical analyses; XRD = powder X-ray diffraction; SEM = scanning electron microscopy; EPMA = electron probe micro analyser; LA-ICPMS = laser ablation inductively coupled plasma mass spectrometry; XANES = X-ray absorption spectroscopy at As or Fe K-edges.

Table S-2 Redox state of arsenic in the serpentinite samples investigated in this study (in mol. % of total As), as obtained from linear combination fits (LCF) of As K-edge XANES spectra using As-bearing reference compounds [a].

Sample number	Mineral fraction	Number of scans	Absorption edge step $\Delta\mu_{fluo}$ [c]	% arsenide $As^{-III\ to\ -I}$	% arsenite $As^{III}O_3$	% arsenate $As^{V}O_4$
CH98A	bulk	8	0.042	<5	40 ± 5	60 ± 3
CH98B	bulk	8	0.022	ND[b]	40 ± 5	60 ± 5
CH146	bulk	15	0.007	22 ± 5	55 ± 5	23 ± 5
TSL16	bulk	4	0.023	ND	28 ± 5	72 ± 5
TSL16	antigorite	5	0.022	<5	33 ± 3	67 ± 5
TSL16	magnetite	2	0.011	ND	<5	95 ± 5
TSL18	bulk	5	0.012	ND	25 ± 3	75 ± 3
TSL19	bulk	5	0.039	43 ± 5	<5	54 ± 5
TSL19	antigorite	1	0.043	47 ± 5	<5	53 ± 5
TSL20	bulk	8	0.022	ND	55 ± 3	45 ± 3
TSL20	magnetite	12	0.006	ND	15 ± 3	85 ± 3
TSL20	magnetite-bis	3	0.006	ND	10 ± 5	90 ± 5

[a] As-bearing reference compound standards used in LCF: As^{V} = arsenate sorbed on ferrihydrite (As5Fh), $NiAsO_4$, $Na_2HAsO_4{\times}7H_2O$, $FeAsO_4{\times}2H_2O$ (scorodite), As_2O_5, arsenic acid aqueous solutions (pH = 2, 10 and 13); As^{III} = As_2O_3 (arsenolite and glass), $NaAsO_2$, arsenious acid aqueous solutions (pH = 5 and 11); As-sulfides: As_2S_3 (orpiment), Cu_3AsS_4 (enargite); As^0 = amorphous native arsenic; $As^{-III\ to\ -I}$: FeAsS (arsenopyrite), $FeAs_2$ (löllingite), NiAsS (gersdorffite), NiAs (nickeline)[1].

[b] ND = not detected (<3% of total As, unless indicated).

[c] Absorption-edge amplitude is a rough indication of total relative As concentration in the studied samples.

[1] As K-edge XAS spectra of reference compounds and serpentinite samples are available upon request to the corresponding author.

Table S-3 Structural parameters of arsenic in serpentinite samples obtained by fitting EXAFS spectra.

Sample number	Mineral fraction	Atom	*N*, atoms	*R*, Å	σ^2, Å^2	$\mathcal{R}$-factor	*k*-range	*R*-range
CH98A	bulk	O	3.6 ± 0.5	1.73 ± 0.03	0.0030	0.025	2.7–12.0	1.1–3.4
		Mg	*1.5 ± 1*	*2.73 ± 0.05*	*0.007f*			
CH98B	bulk	O	3.9 ± 0.5	1.73 ± 0.03	0.0040	0.033	2.7–12.0	1.1–3.4
		Mg	*1.5 ± 1.0*	*2.7 ± 0.1*	*0.007f*			
CH146_RE	bulk	–	–	–	–	–	–	–
TSL16	bulk	O	3.9 ± 1.0	1.72 ± 0.03	0.0025	0.022	2.7–11.2	1.1–3.5
TSL16	magnetite	O	3.9 ± 0.9	1.70 ± 0.02	0.0015	0.040	2.7–10.0	1.1–3.5
TSL16	antigorite	O	3.4 ± 0.5	1.74 ± 0.03	0.0033	0.030	2.7–10.0	1.1–3.5
		±Mg	*1 ± 1*	*2.6 ± 0.1*	*0.007f*			
TSL18	bulk	O	3.6 ± 0.6	1.73 ± 0.02	0.0026	0.028	2.7–10.0	1.1–2.2
TSL19	bulk	O	2.3 ± 0.2	1.70 ± 0.01	0.0020	0.021	2.7–12.8	1.1–3.6
		Ni	3.0 ± 0.5	2.45 ± 0.02	0.0050			
		±S	*<0.4*	*2.20*	*0.005f*			
		±As/Ni	*2 ± 1*	*3.4 ± 0.1*	*0.01f*			
TSL19	antigorite	O	2.0 ± 0.5	1.70 ± 0.01	0.005	0.018	2.7–11.0	1.1–3.6
		Ni	3.0 ± 0.3	2.43 ± 0.02	0.003			
		±As/Ni	*2 ± 1*	*3.4 ± 0.1*	*0.005*			
TSL20	bulk	O	3.3 ± 1.4	1.73 ± 0.03	0.003	0.030	2.7–10.0	1.1–2.2
TSL20	magnetite	O	4.1 ± 1.4	1.70 ± 0.05	0.0015	0.046	2.7–10.0	1.1–2.2
TSL20	magnetite-bis	O	4.0 ± 1.0	1.69 ± 0.02	0.001	0.030	2.7–10.0	1.1–3.5

R = As-neighbour mean distance, *N* = number of neighbours, σ^2 = mean squared displacement of the bond length (relative to σ^2 = 0 adopted in the calculation of reference amplitude and phase functions by FEFF), its typical error is 30–50% of the value; $\mathcal{R}$-factor defines goodness of the total fit in *R*-space. The value of Δe, which is a non-structural parameter accounting for phase shift between experimental spectrum and FEFF calculation, is 9 ± 2 eV for all spectra. Amplitude reduction factor, S_0^2 = 0.9 ± 0.1, as determined from fits of a large number of As-bearing reference compounds recorded in the same experiment. "–" = not fitted due to insufficient EXAFS signal quality; *f* = parameter was fixed in the fit. Values is italic for As outer shells are tentative.

Table S-4 Iron redox and coordination in antigorite fractions from analysis of Fe K-edge XANES spectra [a].

Sample	Pre-edge centroid energy, eV [b]	Fe^{III} (octahedral and tetrahedral) of total Fe, at. %	Fe^{III} tetrahedral of total Fe^{III}, at. %
CH98A	7114.09	66	10
CH98B	7113.90	61	<5
CH146	7.114.14	70	10
TLS16	7113.89	59	<5
TLS18	7114.05	72	<5
TSL19	7113.60	38	<5
TSL20	7113.91	61	<5
Error	±0.1	±5	±5

[a] Numerical algorithms of pre-edge calibration and fitting are from Muñoz *et al.* (2013) and Wilke *et al.* (2001)

[b] Centroid position = intensity-weighted average of the pre-edge components energy positions.

Table S-5 Sources of thermodynamic data for key aqueous species and minerals used in this study.

Chemical species and phases[a]	Data source
Aqueous species	
H_2O, H^+, OH^-, Cl^-, Na^+, $NaCl^0$, $NaOH^0$, KCl^0, K^+, KOH^0, KSO_4^-, $KHSO_4^0$, $NaHSO_4^0$, HS^-, HSO_3^-, SO_3^{2-}, HSO_4^-, SO_4^{2-}, H_2S^0, SO_2^0, H_2^0, O_2^0, Mg^{2+}, $Mg(OH)^+$, Ca^{2+}, $CaOH^+$, $CaCl^+$, $CaCl_2^0$, $CaSO_4$, Fe^{2+}, $FeOH^+$, FeO^0, $HFeO_2^-$, $FeCl^+$, $FeCl_2^0$, Fe^{3+}, $FeOH^{2+}$, FeO^+, $HFeO_2^0$, Ni^{2+}, $NiOH^+$, $Ni(OH)_2^0$, $Ni(OH)_3^-$	Johnson *et al*. (1992 (updated Supcrt database)
HCl^0, $NaSO_4^-$, $NaHS^0$, KHS^0, $NaHSO_4^0$, $S_3^{\bullet-}$	Pokrovski and Dubessy (2015)
$NiCl^+$, $NiCl_2^0$, $NiCl_3^-$	Liu *et al*. (2012)
$Fe(OH)_4^-$	Diakonov *et al*. (1999)
Al^{3+}, $Al(OH)^{2+}$, $Al(OH)_2^+$, $Al(OH)_4^-$, $NaAl(OH)_4^0$	Tagirov and Schott (2001)
$As^{III}(OH)_3^0$, $As^{III}O(OH)_2^-$, $As^{V}O(OH)_3^0$	Perfetti *et al*. (2008)
$H_2As^{V}O_4^-$, $HAs^{V}O_4^{2-}$, $As^{V}O_4^{3-}$	Shock *et al*. (1997)
Solid phases	
native elements S, As, Fe, Ni; most Fe-Mg-Ca-Al-Na-K oxide and silicate minerals	Holland and Powell (2011)
pyrite, pyrrhotite, fayalite, α,β-quartz, magnetite, O_2 ideal gas	Robie and Hemingway (1995)[e]
arsenolite, orpiment, realgar	Pokrovski *et al*. (1996)
Fe sulfarsenides: FeAsS, $FeAs_2$, FeAs	Perfetti *et al*. (2008)
Ni arsenides/arsenates/sulfides: NiAs, Ni_5As_2, $Ni_{11}As_8$, $Ni_3(AsO_4)_2(H_2O)_8$, NiS, Ni_3S_2	Gamsjäger *et al*. (2005)
oxides and arsenates: As_2O_5, AlAs, $AlAsO_4$, $Ca_3(AsO_4)_2$, $Mg_3(AsO_4)_2$	Barin *et al*. (1995)
scorodite $FeAsO_4(H_2O)_2$	Majzlan (2012)
Mg-antigorite $Mg_3Si_{2.125}O_{5.3125}(OH)_{3.875}$	Holland and Powell (2011)
Fe^{II}-antigorite $Fe_3Si_{2.125}O_{5.3125}(OH)_{3.875}$	Merkulova *et al*. (2016)
Fe^{III}-antigorite $Fe_2Si_{2.125}O_{5.3125}(OH)_{3.875}$	This study [c]
Fe^{III}-chrysotile $Fe_2Si_2O_5(OH)_4$	This study [d]
Aqueous species activity coefficient models [b]	
$\log \gamma_i = -A\, z_i^2 \sqrt{I}/(1 + B\, å_i \sqrt{I}) + b\, I + \Gamma_\gamma$, for charged species	Helgeson *et al*. (1981)
$\log \gamma_i = \Gamma_\gamma + b_i\, I$, for uncharged species	
Solid solution models	
olivine: subregular; brucite, orthopyroxene, clinopyroxene, plagioclase, talc, actinolite, chlorite, and garnet: multisite; serpentine: molecular (local charge balance)	Powell (1977)
arsenic in pyrite, $Fe(As,S)_2$	Xing *et al*. (2019)

[a] Thermodynamic properties of H^+ are equal to 0 at all T and P; the reference states for the solid phases and H_2O are unit activity for the pure phase at all T and P; for gases the reference state is ideal gas at 1 bar pressure; for aqueous species, the reference state corresponds to unit activity coefficient for a hypothetical one molal solution whose behaviour is ideal.

[b] A and B are the Debye-Hückel (DH) electrostatic parameters; I is the effective molal ionic strength ($I = 0.5 \sum z_i^2\, m_i$); z_i and $å_i$ are the ionic charge and the distance of the closest approach for KCl or NaCl electrolyte solutions, respectively; b is the extended DH parameter for KCl or NaCl electrolyte solutions; Γ_γ is the mole fraction to molality conversion factor, $\Gamma_\gamma = \log(1 + 0.018m^*)$, where m^* is the sum of the molalities of all solute species. For uncharged aqueous species, b_i is the empirical Setchenov coefficient, which was taken as zero for all neutral species; this yields activity coefficients close to one.

[c] Estimated using the polyhedral contributions approach of Chermak and Rimsdidt (1989) for $\Delta_f G^0_{298K,1bar}$ and assuming that $\Delta_r S$ and $\Delta_r C_p$ equal to 0 at all T and P for the exchange reaction: $Mg_3Si_{2.125}O_{5.3125}(OH)_{3.875}$ (Mg-antigorite) + Fe_2O_3 (hematite) = $Fe^{III}{}_2Si_{2.125}O_{5.3125}(OH)_{3.875}$ (Fe^{III}-antigorite) + 3 MgO (periclase), yielding the following standard thermodynamic properties for Fe^{III}-antigorite: $\Delta_f G^0_{298K,1bar}$ = –3055.54 kJ/mol, $S^0_{298K,1bar}$ = 228.11 J/(mol K), $C_p{}^0$(T in K) = 287.73 + 0.188 × T – 6.9831e6 × T^{-2} J/(mol K), $V^0_{298K,1bar}$ = 105.03 cm^3/mol.

[d] Estimated using the polyhedral contributions approach of Chermak and Rimsdidt (1989) and Klein *et al*. (2009), assuming that $\Delta_r G_{298K,1bar}$, and $\Delta_r S$, $\Delta_r C_p$ and $\Delta_r V$ equal to 0 at all T and P for the exchange reaction: $Al_2Si_2O_5(OH)_4$ (kaolinite) + Fe_2O_3 (hematite) = $Fe^{III}{}_2Si_2O_5(OH)_4$ (Fe^{III}-chrysotile) + Al_2O_3 (corundum), yielding the following standard thermodynamic properties for Fe^{III}-antigorite: $\Delta_f G^0_{298K,1bar}$ = –2959.60 kJ/mol, $S^0_{298K,1bar}$ = 236.90 J/(mol K), $C_p{}^0$(T in K) = 289.32 + 0.141 × T – 5.5913e6 × T^{-2} J/(mol K), $V^0_{298K,1bar}$ = 105.03 cm^3/mol. Plausible uncertainties on $\Delta_f G^0_{298K,1bar}$ values for both Fe^{III}-antigorite and Fe^{III}-chrysotile are ±40 kJ/mol.

[e] FMQ-scale f_{O_2} values used here are according to the Robie and Hemingway (1995) thermodynamic database, which is in excellent agreement (within 0.2 log unit) with high-temperature calibrations (>575 °C) of Myers and Eugster (1983) with pressure correction of Chou (1987). Values of f_{O_2} in water-rock equilibrium simulations of this study are calculated using the equilibrium activity of $O_2{}^0$(aq) and the formal Henry constant O_2(aq) = O_2(gas) from the cited reference sources.

Table S-6 Compositions of the model fluids and rocks used in thermodynamic simulations of this study.

Component	mol/kg	reacted mass, kg
Harzburgite mantle rock [a]		1.0
Olivine, $Mg_{1.8}Fe_{0.2}SiO_4$	5.42	
Orthopyroxene, $Mg_{0.8}Fe_{0.2}SiO_2$	1.43	
Clinopyroxene, $CaMg_{0.9}Fe_{0.1}Si_2O_6$	0.22	
Ni_2SiO_4	0.017	
Pelite-type sediment rock [b]		0.1–0.5
SiO_2	11.24	
Al_2O_3	13.39	
FeO	0.95	
$FeO_{1.5}$	0.09	
K_2O	0.43	
Na_2O	0.085	
CaO	0.042	
MgO	0.545	
H_2O	1.81	
FeS_2	0.083	
FeAsS	0.02	
Seawater		0.1–1.0
H_2O	55.5	
NaCl	0.5	
$MgSO_4$	0.03	

[a] McCollom and Bach (2009); [b] Zhong *et al*. (2015)

Supplementary Figures

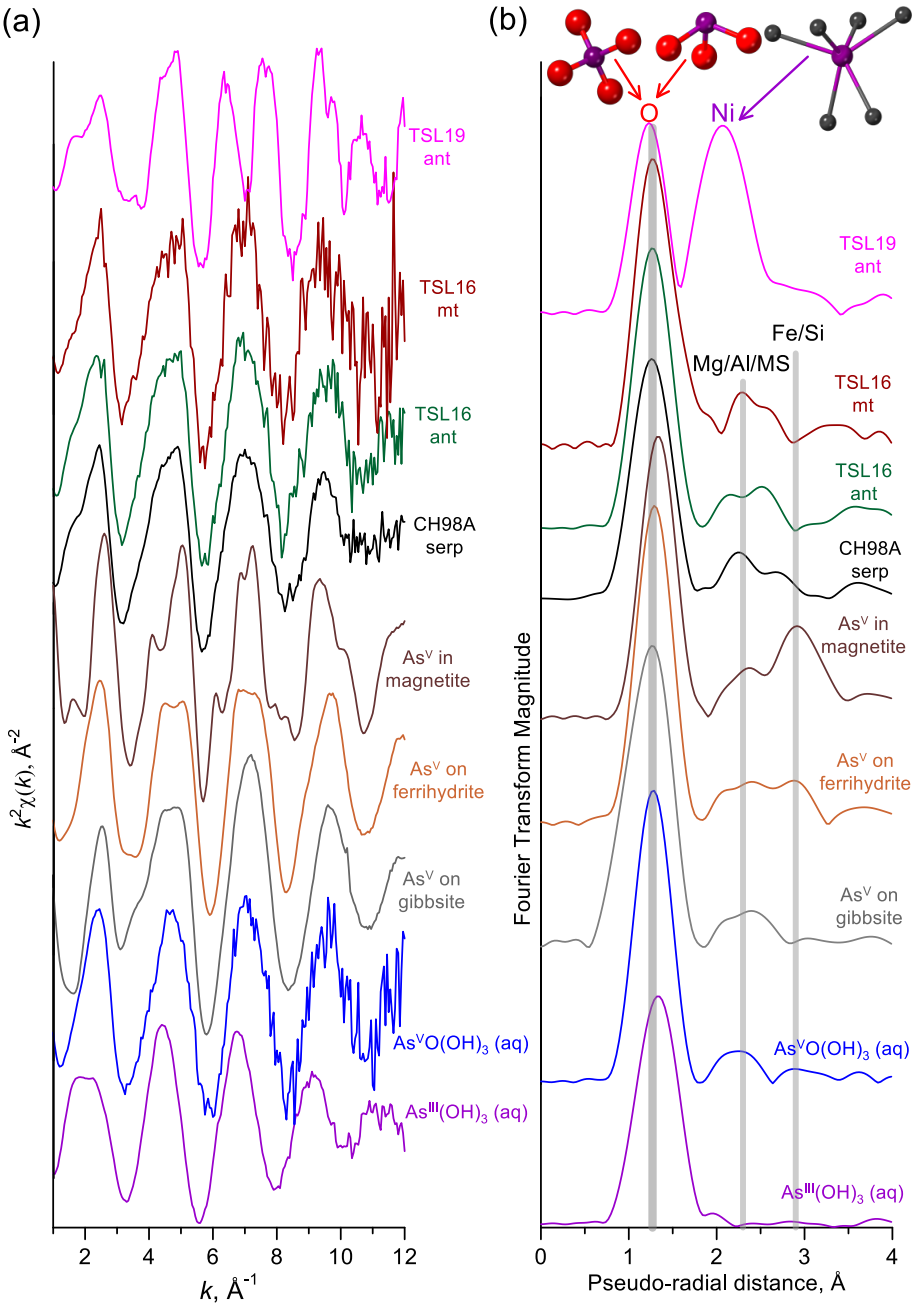

Figure S-1 **(a)** EXAFS spectra (k^2-weighted) at As K-edge, and **(b)** their corresponding Fourier Transform magnitudes of representative serpentinite samples and key reference compounds: arsenious acid As^{III}(OH)$_3$ and arsenic acid As^{V}O(OH)$_3$ aqueous solutions, arsenate incorporated in the magnetite structure (van Genuchten *et al.*, 2019), and arsenate sorbed on ferrihydrite (Cancès *et al.*, 2005) and on gibbsite (Foster and Kim, 2014). Mean positions in *R*-space of major atomic shells around As are indicated by vertical lines in **(b)** (not corrected for phase shift, see Table S-3 and supplementary text for true interatomic distances). Arsenide, arsenide and arsenate first-shell coordination structures are shown by ball-and-stick clusters (As = violet, O = red, Ni = dark grey).

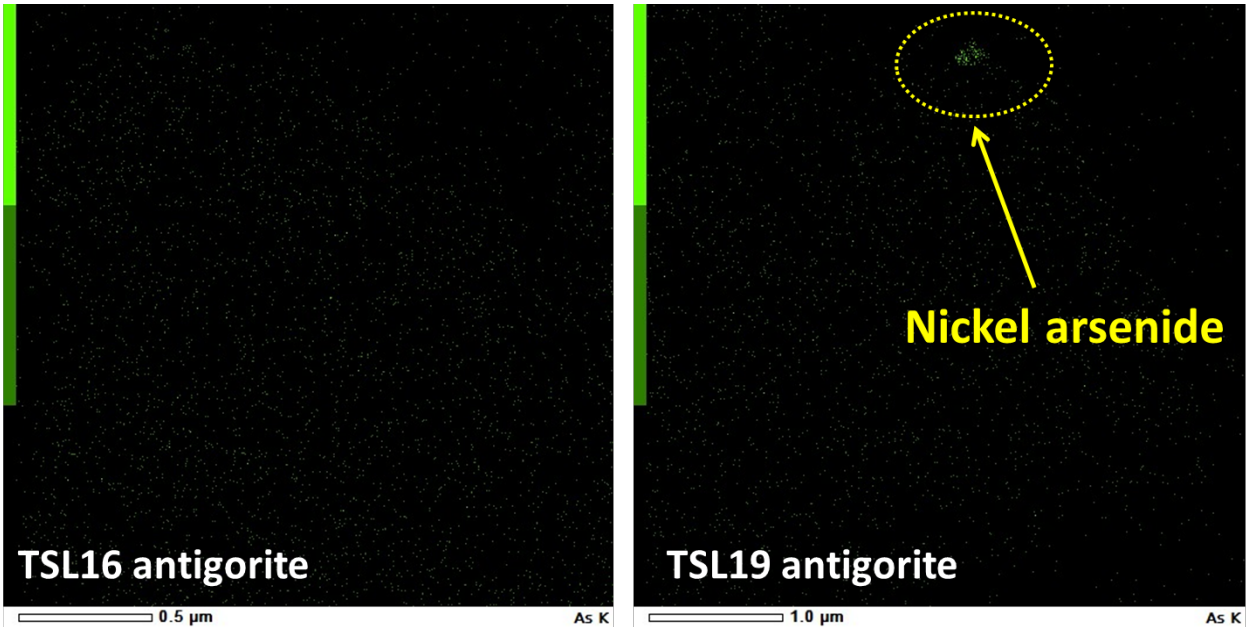

Figure S-2 Transmission electron microscopy (TEM) fluorescence maps at As K-edge of representative antigorite samples (TSL16 and TSL19). Note the absence of detected As-bearing nanoparticles in TSL16 (small single dots are individual illuminated pixels due to background signal), whereas a NiAs-bearing nanoparticle is visible in TSL19 as a group of multiple illuminated pixels (encircled). These findings are in excellent agreement with the bulk antigorite XAS data demonstrating As^{III} and As^{V} to be disseminated in the antigorite structure in TSL16, and the presence of As-Ni bearing phase contributions in TSL19 (Tables S-2 and S-3).

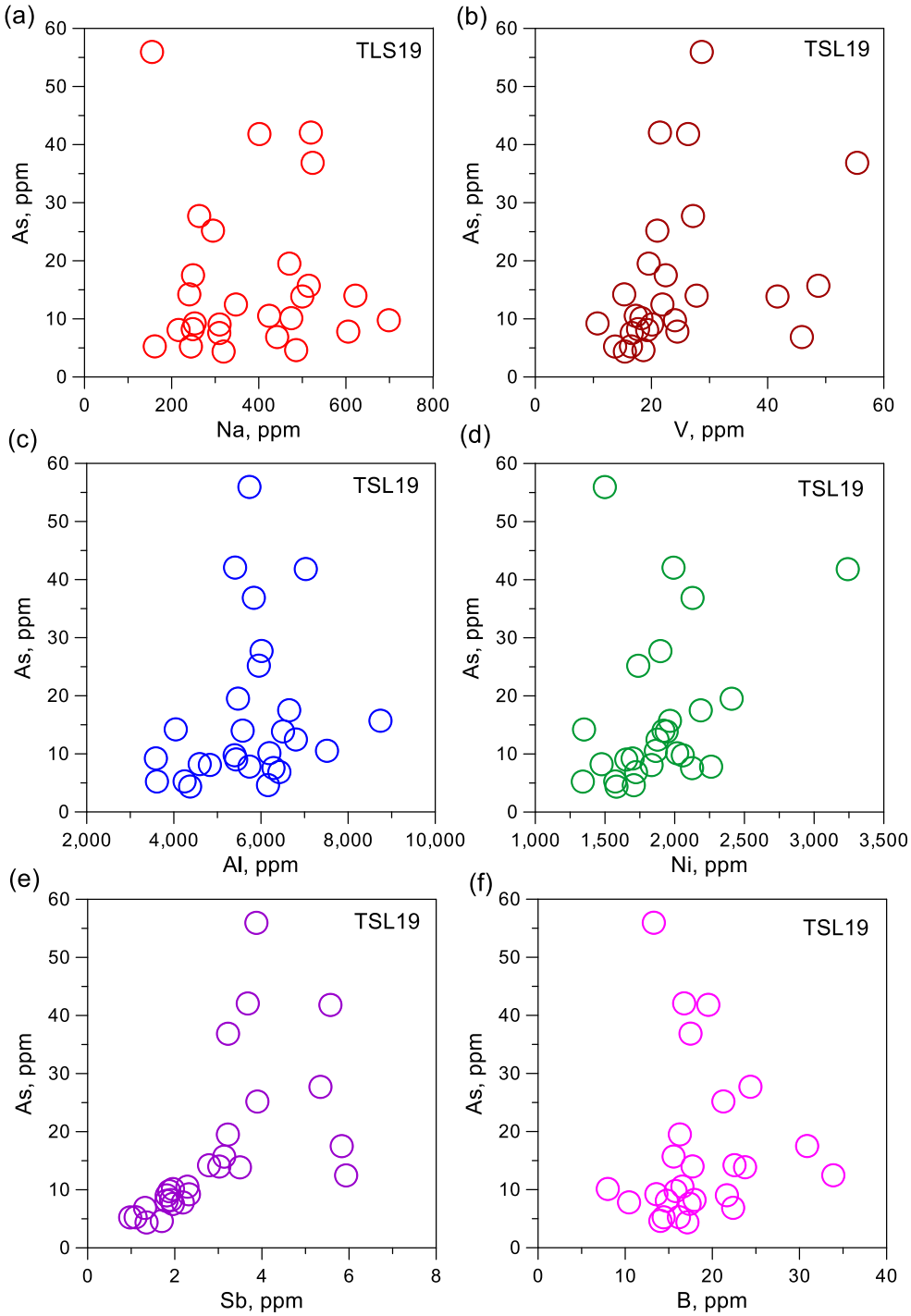

Figure S-3 Scatter plots of arsenic *vs.* the indicated minor and trace elements contents in TSL19 antigorite sample from individual laser spots as probed by LA-ICPMS. Errors are comparable with the symbol size. The lack of apparent correlations of arsenic content with any of those elements (except probably Sb) indicates that arsenic is "decoupled" from these elements that exert no structural/chemical control on As incorporation into antigorite.

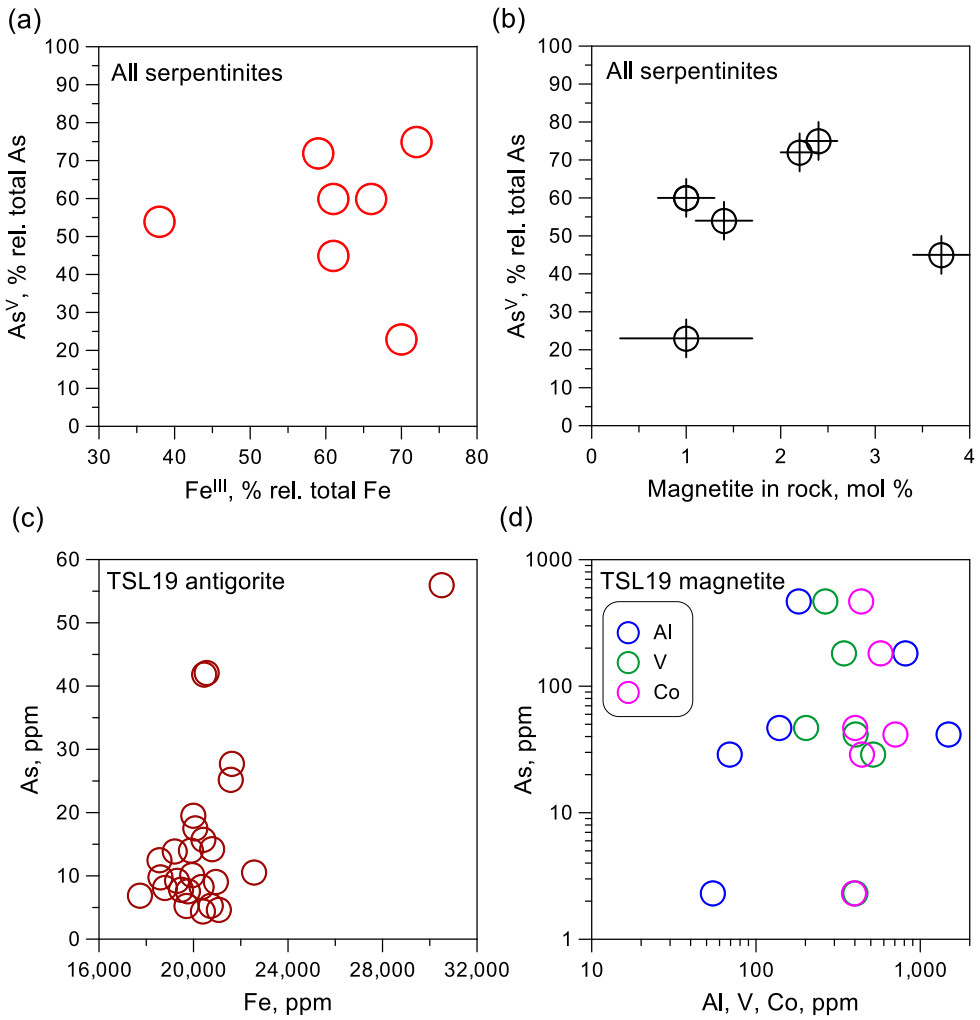

Figure S-4 Arsenic-iron relationships in serpentinite. **(a)** As^V *vs*. Fe^{III} fraction relative to total As and Fe in all antigorite samples as determined by XANES spectroscopy. **(b)** As^V fraction of total As (XANES) *vs*. magnetite mineral fraction in serpentinite rock samples (XRD). **(c)** and **(d)** Total arsenic *vs.* indicated element concentrations in TSL19 antigorite sample from individual laser spots as probed by LA-ICPMS. Errors (unless indicated) are comparable with the symbol size. The lack of any significant correlation of arsenic redox and concentration with Fe and associated elements demonstrates that both As total concentration and redox state are uncorrelated from iron in serpentinite and are not controlled by magnetite.

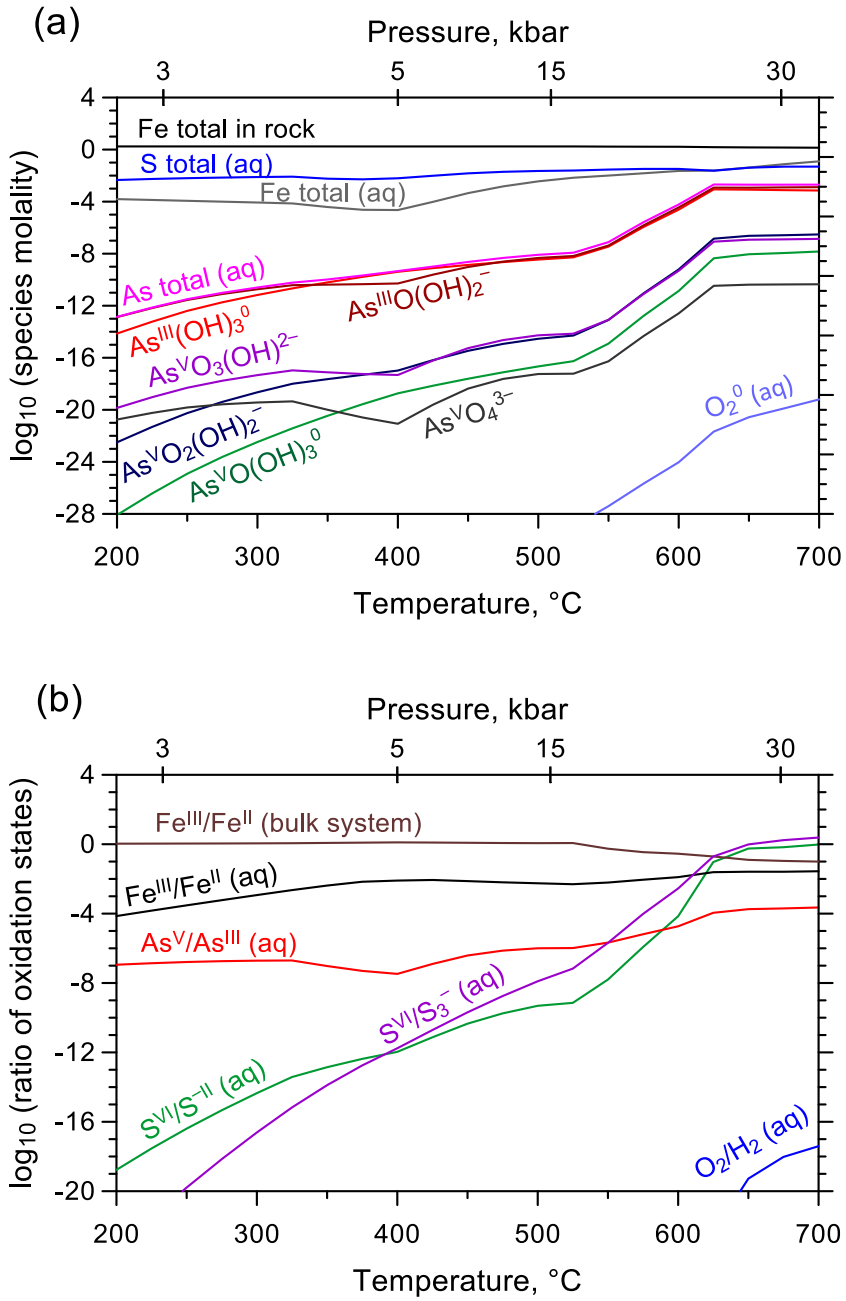

Figure S-5 **(a)** Concentrations of arsenic oxyhydroxide species, total dissolved arsenic, sulfur and iron in the aqueous fluid and total iron in the serpentinite rock (moles per 1 kg of water). **(b)** Ratios of aqueous As^{V}/As^{III}, sulfate/sulfide, trisulfur ion/sulfide and ferric/ferrous iron and molecular oxygen/hydrogen in the fluid, and Fe^{III}/Fe^{II} in the bulk system at equilibrium as a function of temperature, in the example of thermodynamic simulation of serpentinisation in the harzburgite-sediment-water system, along the *T-P* path of Himalayan subduction considered in Fig. 3 of the main text. Note that at the f_{O_2} values of the oxidised fluid generated by out-of-equilibrium serpentinite breakdown, as derived from the As^{V}/As^{III} ratios captured by serpentinite (As^{V}/As^{III}≈1, FMQ+8 to +10, Fig. 3b, main text), the corresponding ratios of aqueous Fe and S redox forms would be proportionally higher that those shown in the figure, largely in favour of the oxidised species. Note, however, that the amount of major redox-sensitive elements in such highly oxidised fluid is too small compared to that of the dominant rock (*e.g.*, there is >10 to 1000 times more Fe^{II} and Fe^{III} in the rock than in the fluid) to leave any significant imprint to the rock in terms of the Fe^{III}/Fe^{II} ratios.

Supplementary Information References

Auzende, A-L., Guillot, S., Devouard, B., Baronnet, A. (2006) Behaviour of serpentinites in convergent context: Microstructural evidence. *European Journal of Mineralogy* 18, 21–33. https://doi.org/10.1127/0935-1221/2006/0018-0021

Barin, I. (1995) *Thermochemical Data of Pure Substances*, 3rd Edition, VHC, Weinheim, Germany. https://doi.org/10.1002/9783527619825

Borisova, A.Y., Pokrovski, G.S., Pichavant, M., Freydier, R., Candaudap, F. (2010) Arsenic enrichment in hydrous peraluminous melts: insights from femtosecond laser ablation - inductively coupled plasma - quadrupole mass spectrometry, and in situ X-ray absorption fine structure spectroscopy. *American Mineralogist* 95, 1095–1104. https://doi.org/10.2138/am.2010.3424

Borisova, A.Y., Zagrtdenov, N.R., Toplis, M.J., Bohrson, W.A., Nédélec, A., Safonov, O.G., Pokrovski, G.S., Ceuleneer, G., Bindeman, I.N., Melnik, O.E., Peter, K.J., Stoll, B., Weis, U., Bychkov, A.Y., Gurenko, A.A., Shcheka, S., Terehin, A., Polukeev, V.M., Varlamov, D.A., Chariteiro, K., Gouy, S., de Parseval, P. (2021) Hydrated peridotite – basaltic melt interaction. Part I: Planetary felsic crust formation at shallow depth. *Frontiers in Earth Sciences* 9, art. 640464. https://doi.org/10.3389/feart.2021.640464

Cancès, B., Juillot, F., Morin, G., Laperche, V., Alvarez, L., Proux, O., Hazemann, J-L., Brown, G.E., Calas, G. (2005) XAS evidence of As(V) association with iron oxyhydroxides in a contaminated soil at a former arsenical pesticide processing plant. *Environmental Science and Technology* 39, 9398–9405. https://doi.org/10.1021/es050920n

Chermak, J.A., Rimsdidt, J.D. (1989) Estimating the thermodynamic properties (ΔG_f^0 and ΔH_f^0) of silicate minerals at 298 K from the sum of polyhedral contributions. *American Mineralogist* 74, 1023–1031.

Chou, I.M. (1987) Oxygen buffer and hydrogen sensor techniques at elevated pressures and temperatures. In: Ulmer, G.C., Barnes, H.L. (Eds.) *Hydrothermal Experimental Techniques*. Wiley, N-Y, 61–99.

Coker, V.S., Gault, A.G., Pearce, C.I., van der Laan, G., Telling N.D., Charnock, J.M., Polya, D.A., Lloyd, J.R. (2006) XAS and XMCD evidence for species-dependent partitioning of arsenic during microbial reduction of ferrihydrite to magnetite. *Environmental Science & Technology* 40, 7745–7750. https://doi.org/10.1021/es060990+

Crerar, D., Wood, S., Brantley, S. (1985) Chemical controls on solubility of ore-forming minerals in hydrothermal solutions. *Canadian Mineralogist* 23, 333–353.

Diakonov, I.I., Schott, J., Martin, F., Harrichoury, J-C., Escalier, J. (1999) Iron(III) solubility and speciation in aqueous solutions. Experimental study and modelling: Part 1. Hematite solubility from 60 to 300 °C in NaOH-NaCl solutions and thermodynamic properties of $Fe(OH)_4^-$(aq). *Geochimica et Cosmochimica Acta* 63, 2247–2261. https://doi.org/10.1016/S0016-7037(99)00070-8

Debret, B., Andreani, M., Muñoz, M., Bolfan-Casanova, N., Carlut, J., Nicollet, C., Schwartz, S., Trcera, N. (2014) Evolution of Fe redox state in serpentine during subduction. *Earth and Planetary Science Letters* 400, 206–218. https://doi.org/10.1016/j.epsl.2014.05.038

Debret, B., Millet, M.-A., Pons, M-L., Bouilhol, P., Inglis, E., Williams, H. (2016) Isotopic evidence of iron mobility during subduction. *Geology* 44, 215–218. https://doi.org/10.1130/G37565.1

Debret, B., Reekie, C.D.J., Mattielli, N., Beunon, H., Ménez, B., Savov, I.P., Williams, H.M. (2020) Redox transfer at subduction zones: insights from Fe isotopes in the Mariana forearc. *Geochemical Perspectives Letters* 12, 46–51. https://doi.org/10.7185/geochemlet.2003

Deschamps, F., Guillot, S., Godard, M., Chauvel, C., Andreani, M., Hattori, K.H. (2010) In situ characterization of serpentinites from forearc mantle wedges: timing of serpentinization and behavior of fluid-mobile elements in subduction zones. *Chemical Geology* 269, 262–277. https://doi.org/10.1016/j.chemgeo.2009.10.002

Evans, B.W., Dyar, D.M., Kuehner, S.M. (2012) Implications of ferrous and ferric iron in antigorite. *American Mineralogist* 97, 184–196. https://doi.org/10.2138/am.2012.3926

Evans, K.A., Frost, B.R. (2021) Deserpentinization in subduction zones as a source of oxidation in arcs: a reality check. *Journal of Petrology* 62, egab016. https://doi.org/10.1093/petrology/egab016

Foster, A.L., Kim, C.S. (2014) Arsenic speciation in solids using X-ray absorption spectroscopy. *Reviews in Mineralogy and Geochemistry* 79, 257–369. https://doi.org/10.2138/rmg.2014.79.5

Gamsjäger, H., Bugajski, J., Gajda, T, Lemire, R.J., Preis, W. (2005) Chemical Thermodynamics of Nickel. In: Nuclear Energy Agency Data Bank, Organisation for Economic Co-operation and Development (Ed.). *Chemical Thermodynamics v. 6*. North Holland Elsevier Science Publishers B.V., Amsterdam.

Guillot, S., Hattori, K.H., de Sigoyer, J. (2000) Mantle wedge serpentinization and exhumation of eclogites: Insights from eastern Ladakh, northwest Himalaya. *Geology* 28, 199–202. https://doi.org/10.1130/0091-7613(2000)28%3C199:MWSAEO%3E2.0.CO;2

Guillot, S., Hattori, K.H., de Sigoyer, J., Nägler, T., Auzende, A.-L. (2001) Evidence of hydration of the mantle wedge and its role in the exhumation of eclogites. *Earth and Planetary Science Letters* 193, 115–127. https://doi.org/10.1016/S0012-821X(01)00490-3

Guillot, S., Mahéo, G., de Sigoyer, J., Hattori, K.H., Pêcher, A. (2008) Tethyan and Indian subduction viewed from the Himalayan high- to ultrahigh-pressure metamorphic rocks. *Tectonophysics* 451, 225–241. https://doi.org/10.1016/j.tecto.2007.11.059

Hattori, K.H., Guillot, S. (2003) Volcanic fronts form as a consequence of serpentinite dehydration in the forearc mantle wedge. *Geology* 31, 525–528. https://doi.org/10.1130/0091-7613(2003)031%3C0525:VFFAAC%3E2.0.CO;2

Hattori, K.H., Guillot, S. (2007) Geochemical character of serpentinites associated with high- to ultrahigh-pressure metamorphic rocks in the Alps, Cuba, and the Himalayas: recycling of elements in subduction zones. *Geochemistry, Geophysics, Geosystems* 8, 1–27. https://doi.org/10.1029/2007GC001594

Hattori, K., Takahashi, Y., Guillot, S., Johanson, B. (2005) Occurrence of arsenic (V) in forearc mantle serpentinites based on X-ray absorption spectroscopy study. *Geochimica et Cosmochimica Acta* 69, 5585–5596. https://doi.org/10.1016/j.gca.2005.07.009

Helgeson, H.C., Kirkham, D.H., Flowers, G.C. (1981) Theoretical prediction of the thermodynamic behavior of aqueous electrolytes at high pressures and temperatures: IV. Calculation of activity coefficients, osmotic coefficients and apparent molal and relative partial molal properties to 600 °C and 5 kb. *American Journal of Science* 281, 1249–1516. https://doi.org/10.2475/ajs.281.10.1249

Holland, T.J.B., Powell, R. (2011) An improved and extended internally consistent thermodynamic dataset for phases of petrological interest, involving a new equation of state for solids. *Journal of Metamorphic Geology* 29, 333–383. https://doi.org/10.1111/j.1525-1314.2010.00923.x

Huhmann, B.L., Neumann, A., Boyanov, M.I., Kemner, K.M., Scherer, M.M. (2017) Emerging investigator series: interdependency of green rust transformation and the partitioning and binding mode of arsenic. *Environmental Science: Processes & Impacts* 19, 1208–1219. https://doi.org/10.1039/C7EM00237H

Johnson, J.W., Oelkers, E.H., Helgeson, H.C. (1992) SUPCRT92: A software package for calculating the standard molal thermodynamic properties of minerals, gases, aqueous species, and reactions from 1 to 5000 bar and 0 to 1000 °C. *Computers & Geoscience* 18, 899–947. https://doi.org/10.1016/0098-3004(92)90029-Q

Keller, N.S., Stefánsson, A., Sigfússon, B. (2014) Arsenic speciation in natural sulfidic geothermal waters. *Geochimica et Cosmochimica Acta* 142, 15–26. https://doi.org/10.1016/j.gca.2014.08.007

Kelly, S.D., Hesterberg, D., Ravel, B. (2008) Analysis of soils and minerals using X-ray absorption spectroscopy. In: Ulery, A.L., Drees, L.R. (Eds.) *Methods of Soil Analysis. Part 5. Mineralogical Methods*, 387–463. Soil Science Society of America, Madison, USA. https://doi.org/10.2136/sssabookser5.5.c14

Klein, F., Bach, W., Jöns, N., McCollom, T., Moskowitz, B., Berquó, T. (2009) Iron partitioning and hydrogen generation during serpentinization of abyssal peridotites from 15°N on the Mid-Atlantic Ridge. *Geochimica et Cosmochimica Acta* 73, 6868–6893. https://doi.org/10.1016/j.gca.2009.08.021

Kodolányi, J., Pettke, T. (2011) Loss of trace elements from serpentinite during fluid-assisted transformation of chrysotile to antigorite - An example from Guatemala. *Chemical Geology* 284, 351–362. https://doi.org/10.1016/j.chemgeo.2011.03.016

Kouzmanov, K., Pokrovski, G.S. (2012) Hydrothermal controls on metal distribution in Cu(-Au-Mo) porphyry systems. In: Hedenquist, J.W., Harris, M., Camus, F. (Eds.) *Society of Economic Geologists Special Publication* 16, 573–618. https://doi.org/10.5382/SP.16.22

Lafay, R., Montes-Hernandez, G., Janots, E, Munoz, M., Auzende A.-L., Gehin, A., Chiriac, R., Proux, O. (2016) Experimental investigation of As, Sb and Cs behaviour during olivine serpentinization in hydrothermal alkaline systems. *Geochimica et Cosmochimica Acta* 179, 177–202. http://dx.doi.org/10.1016/j.gca.2016.02.014

Liu, W., Migdisov, A., Williams-Jones, A. (2012) The stability of aqueous nickel(II) chloride complexes in hydrothermal solutions: Results of UV–Visible spectroscopic experiments. *Geochimica et Cosmochimica Acta* 94, 276–290. https://doi.org/10.1016/j.gca.2012.04.055

Majzlan, J., Drahota, P., Filippi, M., Grevel, K-D., Kahl, W-A., Plášil, J., Boerio-Goates, J., Woodfield, B.F. (2012) Thermodynamic properties of scorodite and parascorodite ($FeAsO_4 \cdot 2H_2O$), kaňkite ($FeAsO_4 \cdot 3.5H_2O$), and $FeAsO_4$. *Hydrometallurgy* 117–118, 47–56. https://doi.org/10.1016/j.hydromet.2012.02.002

Marini, L., Accornero, M. (2010) Erratum to: Predictions of the thermodynamic properties of metal-arsenate and metal-arsenite aqueous complexes to high temperatures and pressures and geological consequences. *Environmental Earth Science* 59, 1601–1606. https://doi.org/10.1007/s12665-009-0369-x

McCollom, T.M., Bach, W. (2009) Thermodynamic constraints on hydrogen generation during serpentinization of ultramafic rocks. *Geochimica et Cosmochimica Acta* 73, 856–875. https://doi.org/10.1016/j.gca.2008.10.032

Merkulova, M., Muñoz, M., Vidal, O., Brunet, F. (2016) Role of iron content on serpentinite dehydration depth in subduction zones: Experiments and thermodynamic modelling. *Lithos* 264, 441–452. https://doi.org/10.1016/j.lithos.2016.09.007

Merkulova, M., Muñoz, M., Brunet, F., Vidal, O., Hattori, K., Vantelon, D., Trcera, N., Huthwelker, T. (2017) Experimental insight into redox transfer by iron- and sulfur-bearing serpentinite dehydration in subduction zones. *Earth and Planetary Science Letters* 479, 133–143. https://doi.org/10.1016/j.epsl.2017.09.009

Maurice, J., Bolfan-Casanova, N., Demouchy, S., Chauvigne, P., Schiavi, F., Debret, B. (2020) The intrinsic nature of antigorite breakdown at 3 GPa: Experimental constraints on redox conditions of serpentinite dehydration in subduction zones. *Contributions to Mineralogy and Petrology* 175, 94. https://doi.org/10.1007/s00410-020-01731-y

Muñoz, M., Vidal, O., Marcaillou, C., Pascarelli, S., Mathon, O., Farges, F. (2013) Iron oxidation state in phyllosilicate single crystals using Fe-K pre-edge and XANES spectroscopy: Effects of the linear polarization of the synchrotron X-ray beam. *American Mineralogist* 98, 1187–1197. https://doi.org/10.2138/am.2013.4289

Myers, J., Eugster, H.P. (1983) The system Fe-Si-O: Oxygen buffer calibrations to 1,500K. *Contributions to Mineralogy and Petrology* 82, 75–90. https://doi.org/10.1007/BF00371177

Nadoll, P., Angerer, T., Mauk, J.L., French D., Walshe J. (2014) The chemistry of hydrothermal magnetite: A review. *Ore Geology Reviews* 61, 1–32. https://doi.org/10.1016/j.oregeorev.2013.12.013

Perfetti, E., Pokrovski, G.S., Ballerat-Busserolles, K., Majer, V., Gibert, F. (2008) Densities and heat capacities of aqueous arsenious and arsenic acid solutions to 350 °C and 300 bar, and revised thermodynamic properties of $As(OH)_3^0$(aq), $AsO(OH)_3^0$(aq), and iron sulfarsenide minerals. *Geochimica et Cosmochimica Acta* 72, 713–731. https://doi.org/10.1016/j.gca.2007.11.017

Piccoli, F., Hermann, J., Pettke, T., Connoly, J.A.D., Kempf, E.D., Vieira Duarte, J.F. (2019) Subducting serpentinites release reduced, not oxidized, aqueous fluids. *Scientific Reports* 9, 19573. https://doi.org/10.1038/s41598-019-55944-8

Pokrovski, G.S., Dubessy, J. (2015) Stability and abundance of the trisulfur radical ion S_3^- in hydrothermal fluids. *Earth and Planetary Science Letters* 411, 298–309. https://doi.org/10.1016/j.epsl.2014.11.035

Pokrovski, G.S., Gout, R., Zotov, A., Schott, J., Harrichoury, J.-C. (1996) Thermodynamic properties and stoichiometry of the arsenic(III) hydroxide complexes at hydrothermal conditions. *Geochimica et Cosmochimica Acta* 60, 737–749. https://doi.org/10.1016/0016-7037(95)00427-0

Pokrovski, G.S., Kara, S., Roux, J. (2002) Stability and solubility of arsenopyrite, FeAsS, in crustal fluids. *Geochimica et Cosmochimica Acta* 66, 2361–2378. https://doi.org/10.1016/S0016-7037(02)00836-0

Pokrovski, G.S., Escoda, C., Blanchard, M., Testemale, D., Hazemann, J-L., Gouy, S., Kokh, M.A., Boiron, M-C., de Parseval, F., Aigouy, T., Menjot, L., de Parseval, P., Proux, O., Rovezzi, M., Béziat, D., Salvi, S., Kouzmanov, K., Bartsch, T., Pöttgen, R., Doert, T. (2021) An arsenic-driven pump for invisible gold in hydrothermal systems. *Geochemical Perspectives Letters* 17, 39–44. https://doi.org/10.7185/geochemlet.2112

Powell, R. (1977) Activity-composition relation for crystalline solutions. In: Fraser, D.G. (Ed.), *Thermodynamics in Geology*. D. Reidel Publishing Company, Dordrecht, 57–65. https://doi.org/10.1007/978-94-010-1252-2_4

Proux, O., Biquard, X., Lahera, E., Menthonnex, J.-J., Prat, A., Ulrich, O., Soldo, Y., Trévisson, P., Kapoujvan, G., Perroux, G., Taunier, P., Grand, D., Jeantet, P., Deleglise, M., Roux, J.-P., Hazemann, J.-L. (2005) FAME: a new beamline for X-ray absorption investigations of very diluted systems of environmental, material and biological interests. *Physica Scripta* T115, 970–973. https://doi.org/10.1238/Physica.Topical.115a00970

Ravel, B., Newville, M. (2005) ATHENA, ARTEMIS, HEPHAESTUS: data analysis for X-ray absorption spectroscopy using IFEFFIT. *Journal of Synchrotron Radiation* 12, 537–541. https://doi.org/10.1107/S0909049505012719

Ryan, P.C., Huertas, F.J., Pincus, L.N., Painter, W. (2019) Arsenic-bearing serpentinite-group minerals: Mineral synthesis with insights for the arsenic style. *Clays and Clay Minerals* 67, 488–506. https://doi.org/10.1007/s42860-019-00040-1

Robie, R.A., Hemingway, B.S. (1995) Thermodynamic properties of minerals and related substances at 298.15 K and 1 bar (10^5 Pascals) pressure and at higher temperatures. *U.S. Geological Survey Bulletin* 2131, 461p. https://doi.org/10.3133/b2131

Schwartz, S., Guillot, S., Reynard, B., Lafay, R., Debret, B., Nicollet, C., Lanari, P., Auzende, A.L. (2013) Pressure–temperature estimates of the lizardite/antigorite transition in high pressure serpentinites. *Lithos* 178, 197–210. https://doi.org/10.1016/j.lithos.2012.11.023

Shock, E.L. Sassani, D.C., Willis, M., Sverjensky, D.A. (1997) Inorganic species in geologic fluids: Correlations among standard molal thermodynamic properties of aqueous ions and hydroxide complexes. *Geochimica et Cosmochimica Acta* 61, 907–950. https://doi.org/10.1016/S0016-7037(96)00339-0

Shvarov, Y.V. (2008) HCh: new potentialities for the thermodynamic simulation of geochemical systems offered by Windows. *Geochemistry International* 46, 834–839. https://doi.org/10.1134/S0016702908080089

Soret, M., Larson, K.P., Cottle, J., Ali, A. (2021) How Himalayan collision stems from subduction. *Geology* 49, 894–898. https://doi.org/10.1130/G48803.1

Sverjensky, D.A., Harrison, B., Azzolini, D. (2014) Water in the deep Earth: The dielectric constant and the solubilities of quartz and corundum to 60 kb and 1200 °C. *Geochimica et Cosmochimica Acta* 129, 125–145. https://doi.org/10.1016/j.gca.2013.12.019

Tagirov, B.R., Schott, J. (2001) Aluminum speciation in crustal fluids revisited. *Geochimica et Cosmochimica Acta* 65, 3965–3992. https://doi.org/10.1016/S0016-7037(01)00705-0

Testemale, D., Hazemann, J.-L., Pokrovski, G.S., Joly, Y., Roux, J., Argoud, R., Geaymond, O. (2004) Structural and electronic evolution of the $As(OH)_3$ molecule in high temperature aqueous solutions: An x-ray absorption investigation. *Journal of Chemical Physics* 121, 8973–8982. https://doi.org/10.1063/1.1785150

Testemale, D., Brugger, J., Liu, W., Etschmann, B., Hazemann, J.-L. (2009) *In-situ* X-ray absorption study of Iron(II) speciation in brines up to supercritical conditions. *Chemical Geology* 264, 295–310. https://doi.org/10.1016/j.chemgeo.2009.03.014

Testemale, D., Pokrovski, G.S., Hazemann, J-L. (2011) Speciation of As^{III} and As^{V} in hydrothermal fluids by *in situ* X-ray absorption spectroscopy. *European Journal of Mineralogy* 23, 379–390. https://doi.org/10.1127/0935-1221/2011/0023-2104

van Genuchten, C.M., Behrends, T., Dideriksen, K. (2019) Emerging investigator series: interdependency of green rust transformation and the partitioning and binding mode of arsenic. *Environmental Science: Processes & Impacts* 21, 1459–1476. https://doi.org/10.1039/C9EM00267G

van Genuchten, C.M., Behrends, T., Stipp, S.L.S., Dideriksen, K. (2020) Achieving arsenic concentrations of <1 µg/L by Fe(0) electrolysis: The exceptional performance of magnetite. *Water Research* 168, 115170. https://doi.org/10.1016/j.watres.2019.115170

Vils, F., Müntener, O., Kalt, A., Ludwig, T. (2011) Implications of the serpentine phase transition on the behaviour of beryllium and lithium-boron of subducted ultramafic rocks. *Geochimica et Cosmochimica Acta* 75, 1249–1271. https://doi.org/10.1016/j.gca.2010.12.007

Wilke, M., Farges, F., Petit, P-E., Brown, Jr., G.E., Martin, F. (2001) Oxidation state and coordination of Fe in minerals: An Fe K-XANES spectroscopic study. *American Mineralogist* 86, 714–730. https://doi.org/10.2138/am-2001-5-612

Xing, Y., Brugger, J., Tomkins, A., Shvarov, Y. (2019) Arsenic evolution as a tool for understanding formation of pyritic gold ores. *Geology* 47, 335–338. https://doi.org/10.1130/G45708.1

Zhong, R., Brugger, J., Tomkins, A.G., Chen, Y., Li, W. (2015) Fate of gold and base metals during metamorphic devolatilization of a pelite. *Geochimica et Cosmochimica Acta* 171, 338–352. https://doi.org/10.1016/j.gca.2015.09.013